Scale effect and two-phase flow in a thin hydrophobic porous layer. Application to water transport in gas diffusion layers of proton exchange membrane fuel cells

M. Rebai [a,b], M. Prat [a,b,*]

[a] Université de Toulouse, INPT, UPS, IMFT, Avenue Camille Soula, 31400 Toulouse, France
[b] CNRS, IMFT, 31400 Toulouse, France

ABSTRACT

Pore network simulations are performed to study water transport in gas diffusion layers (GDLs) of polymer electrolyte membrane fuel cells (PEMFCs). The transport and equilibrium properties are shown to be scale dependent in a thin system like a GDL. A distinguishing feature of such a thin system is the lack of length scale separation between the system size and the size of the representative elementary volume (REV) over which are supposed to be defined the macroscopic properties within the framework of the continuum approach to porous media. Owing to the lack of length scale separation, two-phase flow traditional continuum models are expected to offer poor predictions of water distribution in a GDL. This is illustrated through comparisons with results from the pore network model. The influence of inlet boundary conditions on invasion patterns is studied and shown to affect greatly the saturation profiles. The effects of GDL differential compression and partial coverage of outlet surface are also investigated.

© 2009 Elsevier B.V. All rights reserved.

1. Introduction

Fuel cells are attracting increasing attention as an important energy converter and many groups work throughout the world in order to improve their performances, efficiency, reliability, manufacturability and cost-effectiveness. In particular, polymer electrolyte membrane (PEM) fuel cells are under intense studies and development. One well identified limitation of the PEMFC performances at high current densities originates in the blockage of the pores of the GDL (Gas diffusion layer) by liquid water. This blockage constraints the reactant transport to the catalyst layers. This problem has motivated many studies on the modelling of two-phase transport in the GDL. One can distinguish three main approaches: continuum models, pore network models, direct simulations. Continuum models refer to the traditional models widely used in many applications involving porous media; these notably include petroleum engineering and subsurface hydrology. The porous medium is treated as a hypothetical effective continuum and the models involve volume-averaged quantities such as saturation and rely on phenomenological relationships such as the generalized Darcy's law. Key parameters in this approach are the permeability, relative permeabilities and the capillary pressure–saturation curve. Despite recurrent questions about the relevant functional forms to be used for these parameters for the fibrous media forming the GDLs, this approach has been used extensively for modelling water-gas flows in GDLs, e.g. [1–3] and references therein. As discussed for example in [4], there are however serious concerns about using this type of model for a thin system like a GDL, especially due to the lack of a significant length scale separation between the pore scale and the GDL thickness. This has motivated in part the two main alternative approaches listed above. Direct simulations aim at computing the two-phase flow by solving directly the problem at the pore scale. This can be performed using for example a Lattice Boltzmann model, [5]. Although interesting for a better understanding of two-phase flow in a complex microstructure such as the one of a GDL, direct simulations are of limited practical use because of the large computing resources needed. In this respect, pore network models are much more efficient and appear as a good option not only for determining the parameters needed in the traditional continuum approach, e.g. [6], but also as a valuable tool for gaining a better understanding of the phenomena occurring at the pore network scale as well as for possibly improving the design of GDLs, e.g. [7–9] and references therein. In this paper, we also use pore network models. The main objective is to evaluate what can be expected from continuum models and also to study several effects on water transport in GDL. These include the scale effect associated with the thin nature of GDL, the injection condition at the GDL inlet and the

* Corresponding author at: Université de Toulouse, INPT, UPS, IMFT, Avenue Camille Soula, 31400 Toulouse, France. Tel.: +33 561285883; fax: +33 561285899.
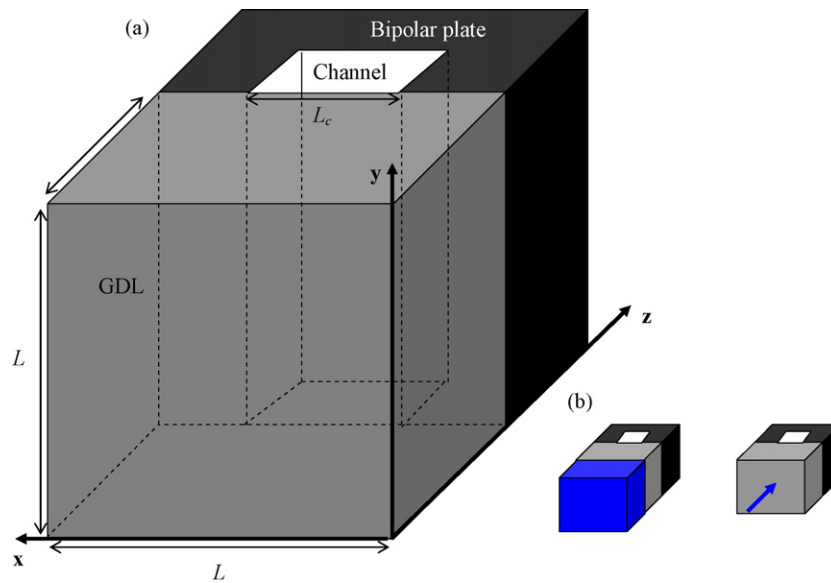E-mail address: prat@imft.fr (M. Prat).

Fig. 1. (a) Sketch of GDL unit cell. (b) The two injection conditions considered in the paper: GDL in contact with a reservoir at uniform pressure, injection from one single pore located in the centre of GDL inlet surface. These boundary conditions are referred to as the surface injection b.c. and one point injection b.c., respectively.

screen effect due to the fact that only a fraction of the GDL surface adjacent to the bi-polar plate is in contact with the gas channels. Impact of possible effects of GDL differential compression is also investigated.

The paper is organized as follows: first we recall in Section 2 some basic results on drainage in porous media so as to determine the most likely two-phase flow regime in a GDL. A brief discussion about water injection in the GDL is presented in Section 3. In

Fig. 2. Schematic of cubic pore network. The size of the network shown here is $6 \times 6 \times 2$ whereas a $40 \times 40 \times N$ with $N \in [4,40]$ is used for the simulations presented in the present study. For simplicity, the pore size and the throat size shown here are uniform. Actually the throat and pore sizes are randomly distributed as explained in the text.

Section 4, we concentrate on finite size effects in a system of large aspect ratio presumably representative of a GDL unit cell. In Section 5, we explore the impact of screen and compression effects. Section 6 is devoted to a brief investigation of a different scenario in which water enters the GDL from an isolated source rather than from all the pores in contact with the MPL (Microporous layer, which is considered as a layer distinct from the GDL in this paper and not as a part of the GDL) or the Catalyst layer (CL). Some comparisons between the continuum model and pore network simulations are presented in Section 7. Implications of the results as well as possible impacts of additional effects (mixed wettability, GDL anisotropy) are discussed in Section 8.

Before going into the details of the various sections, the configuration and the assumptions considered are presented. Throughout this paper, we assume for simplicity that the porous matrix is hydrophobic (as in many previous studies) and that the GDL microstructure is isotropic (assumption often taken with the continuum models). We are aware that these assumptions can be questioned and this will be briefly considered in Section 8.

Also we do not consider all the GDL but restrict our attention to a sub-region of the GDL referred to as a unit cell or a representative domain, see Fig. 1. Noting that the GDL is in contact with the bipolar plate in which, at least for the most common designs, regularly spaced channels are etched, we take the distance L between two channels as representative size of a GDL unit cell in the in-plane direction. Hence as a reasonable unit cell of the system GDL/bipolar plate, we consider a porous domain of size $L \times L \times \ell$ where ℓ is the GDL thickness. Representative values of L and ℓ are $L \approx 2\,mm$ and $\ell \approx [170–400]\,\mu m$, e.g. [10]. The diameter of fibres forming the GDL is typically of the order of 10 μm whereas the mean pore size is on the order of 50–60 μm, [6,11]. Hence, measured in pore size, a GDL is typically less than 10 pore sizes thick whereas L is on the order of 40 pore sizes. Compared to most other porous materials, a very particular feature of GDL is thus to be a thin system, not so much in terms of aspect ratio, i.e. $\ell < L$, but because there are only a few pores across the GDL thickness.

As discussed in [4], the details on how water is produced within the catalyst layer and reaches the GDL are still somewhat unclear. As in most of the previous works on the subject, we assume that water enters the GDL in liquid phase from the surface of the GDL in contact with either the microporous layer, if any, or the catalyst
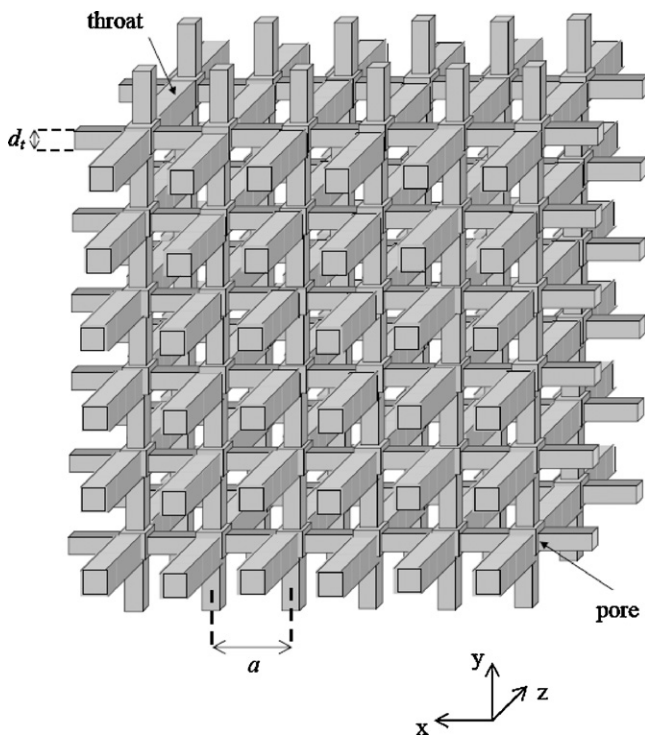
layer. We assume that the GDL is dry initially and we are mainly interested in the water invasion process in this initially dry GDL.

As mentioned before the study is based on pore network simulations. For simplicity, we consider a cubic network. As sketched in Fig. 2, pores of cubic shape are regularly placed on a 3D cartesian grid (with a denoting the lattice spacing). Two first neighbour pores are linked by a channel of square cross-section. Such a channel is referred to as a bond or throat. The pore size d_p (respectively the throat cross section side length d_t), which corresponds to the diameter of the largest sphere inscribed within the pore, is randomly distributed according to a uniform probability law in the range $[d_{pmin}, d_{pmax}]$ (respectively in the range $[d_{tmin}, d_{tmax}]$ with the constraint $d_{tmax} \leq d_{pmin}$). Simulations presented in what follows have been performed with $a = 50\,\mu m$, $d_{pmax} = 46.5\,\mu m$, $d_{pmin} = 34\,\mu m$, $d_{tmax} = 34\,\mu m$, $d_{tmin} = 20\,\mu m$. These values are representative of pore size distributions in GDL, e.g. [6].

The network size is characterized by the number of pores placed in each direction. In accordance with the representative values given above, we consider $40 \times 40 \times N$ networks with N varying in the range [4,40] (with a lattice spacing of $50\,\mu m$, $N = 4$ corresponds for example to a GDL thickness of $200\,\mu m$).

The water invasion process considered in what follows (see Section 2) is sensitive to the particular realization of the network considered (since the pore and throat sizes are random variables, a realization of the network refers to one particular random drawing of pore and throat sizes). As a result, ensemble averaging is needed to obtain the mean behaviour of a given variable of interest. Unless otherwise mentioned, 100 such realizations of each considered network have been typically generated to obtain the results presented in this paper.

2. Theory of drainage and thin systems

When water displaces a gas in a hydrophobic system, water is the non-wetting fluid and the gas is the wetting one. In the porous media literature, e.g. [12], such a process, i.e. the immiscible displacement of a wetting fluid by a non-wetting one is referred to as drainage. When the gravity effects can be neglected, a reasonable assumption in the present context, three main asymptotic invasion regimes can be distinguished depending on the values of the capillary number Ca (which is the ratio between viscous forces acting at the pore scale in water and capillary forces, $Ca = \mu_{nw}U/\gamma \cos\theta_w$, U is a reference velocity, where γ is the surface tension, μ_{nw} is the liquid water dynamic viscosity, θ_w is the contact angle taken in the wetting fluid (air)) and the ratio of dynamic viscosities of the two fluids M, $M = \mu_w/\mu_{nw} \sim 10^{-3}$ for the water/air system, [13,14]. These regimes are the invasion percolation (IP) regime (very low Ca), the capillary-viscous fingering regime (very high M and Ca) and the compact regime (very low M and high Ca). As discussed in [4], the capillary number can be expressed here as $Ca = \mu_{nw}IM_{H_2O}/\gamma \cos\theta_w 2F\rho_{nw}$ where F is the Faraday's constant, M_{H_2O} is the water molecular weight, ρ_{nw} is the liquid water density and I is the current density. With $I = 1\,A\,cm^{-2}$ and $\theta_w = 70°$ (see [4] for a discussion about the value of contact angle), this leads to $Ca \sim 10^{-7}$ to 10^{-8}, a low value presumably consistent with the IP regime. However as pointed out in [14] and [15], the estimate of the capillary number is not sufficient to determine which regime is prevailing. As discussed in [14], the IP regime is expected only for system of size lower than the length X_e (measured in lattice unit a) which is given by,

$$c\frac{Ca}{\Sigma}X_e^{1+\zeta+v(D-1)/v} \approx \beta \qquad (1)$$

where $D = 2.52$ (D is the mass fractal dimension of the percolation cluster), $v = 0.88$, $\zeta = 1.12$ (v and ζ are the conductance and correlation exponents of the percolation theory, [16]), $\beta \approx 0.01$, Σ is the
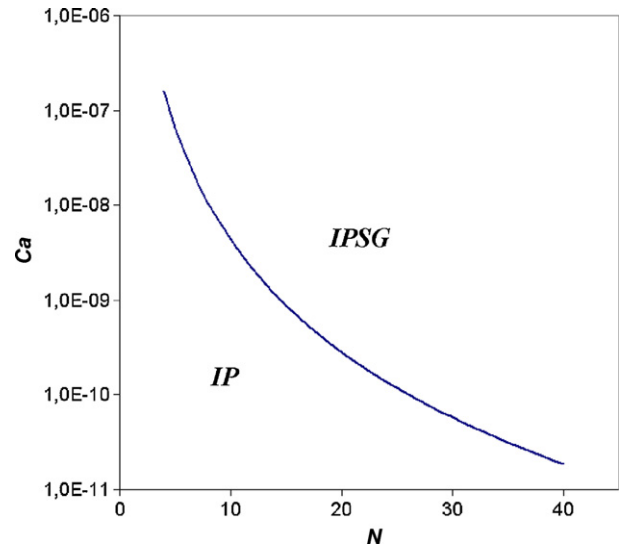

Fig. 3. Evolution of capillary number Ca marking the transition between a pure IP regime and the regime IPSG where viscous effects cannot be ignored as a function of pore-network thickness.

dimensionless standard deviation of the throat size distribution. For a uniform distribution, $\Sigma = 2(d_{t\,max} - d_{t\,min})/\sqrt{12}(d_{t\,max} + d_{t\,min})$. In Eq. (1), c is a constant which has be computed for our network and is found to be $c \approx 40$. As shown in [14] or [15], Eq. (1) is obtained by estimating the evolution of capillary pressure induced by viscous effects along an IP cluster and corresponds here to the special case where the pressure drop in the less viscous fluid (the gas) is neglected. From Eq. (1), we can estimate the evolution of capillary number above which the displacement ceases to be a pure IP displacement. The results are shown in Fig. 3 where IPSG stands for invasion percolation in a stabilizing gradient and corresponds to the regime where viscous effects are non-negligible. As can be seen from Fig. 3, the values of Ca 10^{-7} to 10^{-8} estimated before correspond in fact to the values marking the limit of the IP regime for $N \leq 10$, which is the range of N expected for the GDL. Hence this confirms that the IP model is a valuable tool to simulate the displacement of gas by water in a GDL. However, one should keep in mind that the system operates close to the limit of validity of the IP model. Therefore, viscous effects might become non-negligible if higher liquid flow rates were to be considered (because of, for instance, improvements in the fuel cell performances).

3. Injection conditions

As mentioned before, the exact conditions under which water is produced in the active layer and reaches the GDL (after travelling across the microporous layer (MPL) if any) are still somewhat unclear, e.g. [1,17]. As in most previous investigations, we assume here that water enters the GDL in liquid phase and that condensation of water vapour can be neglected. In the traditional application of IP model, the entrance surface of the porous medium is supposed to be in contact with a reservoir of non-wetting fluid at uniform pressure. However, the situation may be different for a GDL in an operating fuel cell owing to the presence of the adjacent porous layer, i.e. the active layer or the MPL. As interestingly pointed out in [9] and [17], more realistic conditions could be multiple injections through each pore of the GDL entrance surface or only through some of them. Since the traditional condition is widely used and is presumably representative of, at least, ex-situ experiments, e.g. [18], most of our simulations will rely on this condition. However, we will consider in Section 6 also the extreme case of the injection

through one single injection pore so as to have some indication of the possible impact of boundary condition on invasion pattern and pore occupancy at breakthrough. These two cases are sketched in Fig. 1 and are referred to as the "surface injection" condition and the "one point injection "condition, respectively.

4. Finite size effects in thin system

One major feature of one invasion percolation pattern is to be a fractal pattern. As a result, many quantities are scale dependent, especially at breakthrough (BT), i.e. when water reaches for the first time the GDL/bipolar plate interface. This scale dependence is illustrated here through the consideration of several quantities of interest, ignoring throughout this section the screen effect mentioned in the introduction, i.e. the water injected on one side of the GDL is free to exit from any throat present on the GDL opposite surface (with the notation used in Section 5, this corresponds to $\Phi = 1$, where Φ is the fraction of the GDL unit cell surface on the bipolar plate side in contact with the gas channel).

4.1. Overall saturation at breakthrough

The overall water saturation S_{BT} at breakthrough is the volume fraction of pore space in the $40 \times 40 \times N$ network which is occupied by water at breakthrough whereas $\langle S \rangle_{BT}$ is the overall water saturation at breakthrough averaged over many realizations (500 for $N = 4$, 350 for $N = 10$ and 250 for $N > 10$). To compute S_{BT} for a particular realization, we use the IP algorithm without trapping (trapping is negligible in 3D network up to breakthrough), as described for example in [4]. For a porous domain $L \times L \times L$ where L is measured in lattice unit, $\langle S \rangle_{BT}$ scales as, e.g. [16],

$$\langle S \rangle_{BT} \propto \frac{1}{L^{0.48}} \quad (2)$$

Hence the fraction of pore space $1 - \langle S \rangle_{BT}$ left available for the gaseous reactant to reach the catalyst layer increases with the size of the domain (measured in lattice spacing unit).

Consider now a $L \times L \times N$ pore network of fixed lateral extension L ($L = 40$ in our case) and study the influence of N on $\langle S \rangle_{BT}$. Pore network simulations based on the IP algorithm lead to the results shown in Fig. 4 ("surface injection" results in Fig. 4). As can be seen, $\langle S \rangle_{BT}$ increases with N. Interestingly, it can be seen from Fig. 4 that $\langle S \rangle_{BT}$ is very low, close to 4%, for the thinnest system considered (4 pore sizes thick) and increases rapidly with thickness up to 13% for the 40 pore sizes thick system (for which $\langle S \rangle_{BT}$ is given by Eq. (2) with $L = 40$). Hence these results indicate that the thinnest the GDL (expressed in lattice unit), the smallest the fraction of blocked pores at breakthrough. Interestingly, the fraction of pore volume available to the gas can be considered as high whatever the GDL thickness in the range of thickness investigated, which is a clear indication that the IP regime is well adapted for draining the water across the GDL with a high degree of accessibility to the catalyst layer for the gas. Also, a typical feature of thin system is the significance of statistical fluctuations as exemplified by the error bars in Fig. 4.

4.2. Capillary pressure curve

As mentioned in the introduction, the capillary–pressure curve $P_c(S)$ (or equivalently $P_c(S_g)$ where $S_g = 1 - S$) is one of the key parameters entering into the traditional continuum models. As exemplified for example in [6], pore network models can be used to determine $P_c(S)$. To this end, we used the algorithm described hereafter, which also relies on IP concepts. Due to the random fluctuations, $P_c(S)$ has to be determined over many realizations of the network. For a given realization, we start with a dry network and determine the overall capillary pressure as a function of S for suc-
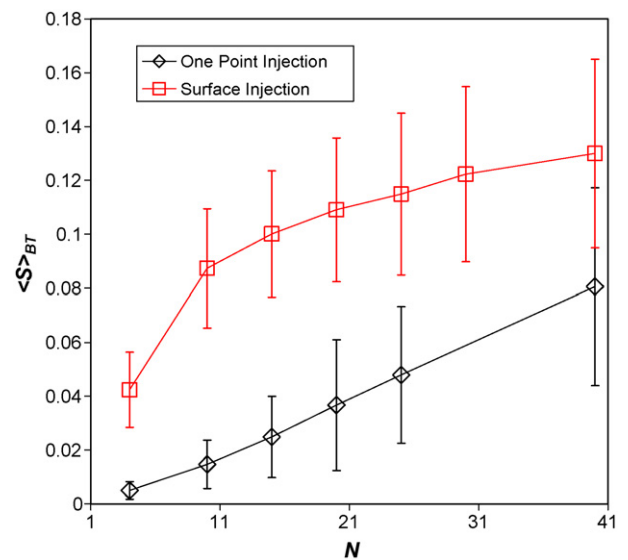

Fig. 4. Evolution of mean overall water saturation at breakthrough as a function of network thickness for the two boundary conditions depicted in Fig. 1. The error bars represent ±1 standard deviation around the mean values over the number of realizations considered.

cessive states of hydrostatic equilibrium corresponding to small increment dP_{nw} in the non-wetting fluid pressure (the wetting fluid pressure is maintained constant). The algorithm used to determine the saturation evolution right after a non-wetting fluid pressure increment reads:

1. Identification of each bond that can be invaded, that is each wetting fluid bond such that its capillary pressure threshold p_c is lower than the pressure difference $P_{nw} - P_w$ between the two fluids.
2. Identification of clusters formed by the bonds identified in (1) using the Hoshen–Kopelman algorithm [19].
3. Identification of clusters among the clusters identified in (2) in contact with the invading non-wetting phase.
4. Invasion of all clusters identified in (3).
5. Computation of overall saturation.

Note that trapping is not taken into account here as well as in the rest of the paper, see for example [20] and references therein for more details on this aspect. The local capillary pressure threshold p_c of a throat is expressed using the Young-Laplace equation as

$$p_c = \frac{4\gamma \cos \theta_w}{d_t} \quad (3)$$

Using this algorithm for many realizations (see Section 4.1 for the details on the number of realizations generated) leads to the results shown in Fig. 5. As can be seen from Fig. 5, the capillary pressure curve is thickness dependent but this dependence is only marked in the region of high gas saturation, i.e. near breakthrough. The evolution of $\langle P_c(S_g) \rangle$ in this range of saturation tends to be steeper as N increases. A detailed view of this evolution is shown in Fig. 5b together with error bars corresponding to ±1 standard deviation around the mean values. These results suggest that the experimental measurement of capillary pressure curve in a thin system should be performed with the thin system as it is, i.e. determining for example $P_c(S_g)$ for a thick system formed by a sandwich of several layers of the thin system is not a good idea if an accurate description of $P_c(S_g)$ for S_g close to 1 is sought. This region of the capillary curve is expected to be a very sensitive region for the continuum model if one wishes to describe the invasion of water in a dry hydrophobic GDL with this type of model (this is not, however, the main prob-
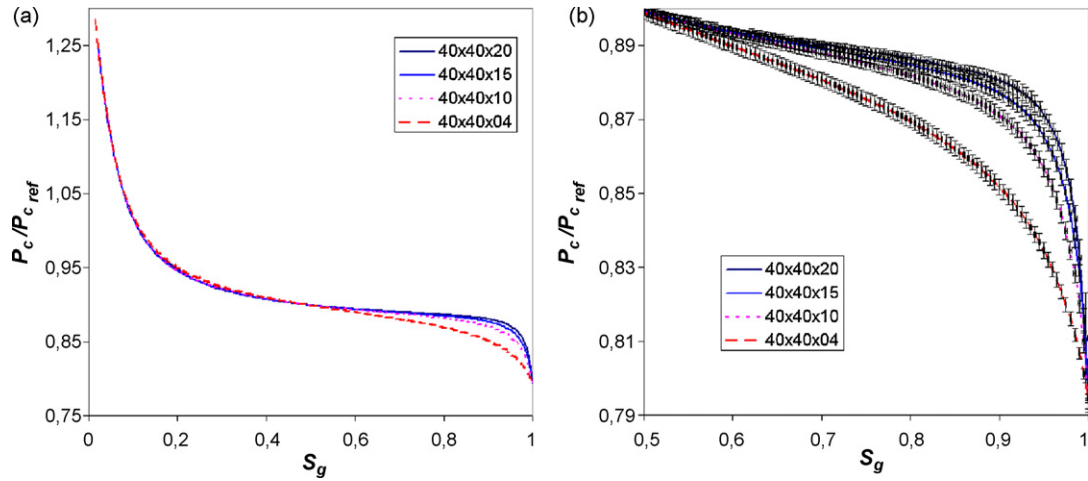
Fig. 5. (a) Influence of network thickness on capillary pressure curve. (b) Detailed view of capillary pressure curve for the high overall gas saturation, the error bars represent ± 1 standard deviation around the mean values over the number of realizations considered. P_{cref} is the capillary pressure threshold given by Eq. (3) for $d_t = \bar{d}_t = (d_{t\max} + d_{t\min}/2)$.

lem with the continuum models as discussed in Section 7). This is due to the fact that the derivative dP_c/dS is one of the parameters of the continuum models. As can be seen from Fig. 5, dP_c/dS tends to diverge as $S_g \rightarrow 1$. This issue is however beyond the scope of the present paper and will be addressed in a forthcoming work (see however Sections 7 and 8 below).

4.3. Permeability and relative permeabilities

The intrinsic permeability and the relative permeabilities are also important parameters of continuum models. To determine the permeability and relative permeabilities of the network, local hydraulic conductances must be assigned to each throat and pore. As in [6], the local conductance of a throat or a pore is expressed as

$$g = \frac{d^4}{14.03 l} \qquad (4)$$

where d is the pore or throat size and l is the pore or throat length. The local flow rate q between two pores is expressed as

$$q = \frac{g_T}{\mu} \Delta P \qquad (5)$$

where μ is the dynamic viscosity of the considered fluid and g_T is the hydraulic conductance between the two pores obtained as the harmonic average of the conductances of the two half pores and the

throat over which there exists the pressure difference ΔP. The procedure is exactly similar to the one described in [6], where more details can be found. Expressing the mass conservation equation over each pore yields a system of linear equations that is solved numerically. As boundary conditions, arbitrary pressures P_{en} and P_{ex} are prescribed on inlet and outlet surfaces of network. This yields the total flow Q over the network. Once Q is determined, the permeability K of the network is found from Darcy's law:

$$Q = \frac{K}{\mu} \frac{P_{en} - P_{ex}}{\ell} \qquad (6)$$

In our case, this gives $\langle K \rangle \approx 4.3 \times 10^{-11}$ m^2 without significant variations with the size N of network.

For determining the relative permeabilities (k_r), we combine the procedure described in Section 4.2 to determine the fluids distribution within the network and the computation of permeability described above. For example the effective permeability $K k_r$ of one fluid is determined using the same procedure as for the intrinsic permeability except that only the sub-network corresponding to this fluid is considered. Again more details on this type of computation can be found in [6].

Not surprisingly, Fig. 6 shows that the relative permeabilities (averaged over the same number of realizations as for $\langle S \rangle_{BT}$ and $\langle P_c(S_g) \rangle$) are network thickness dependent. Again the change is quite significant when the network size varies from 4 to 10 and
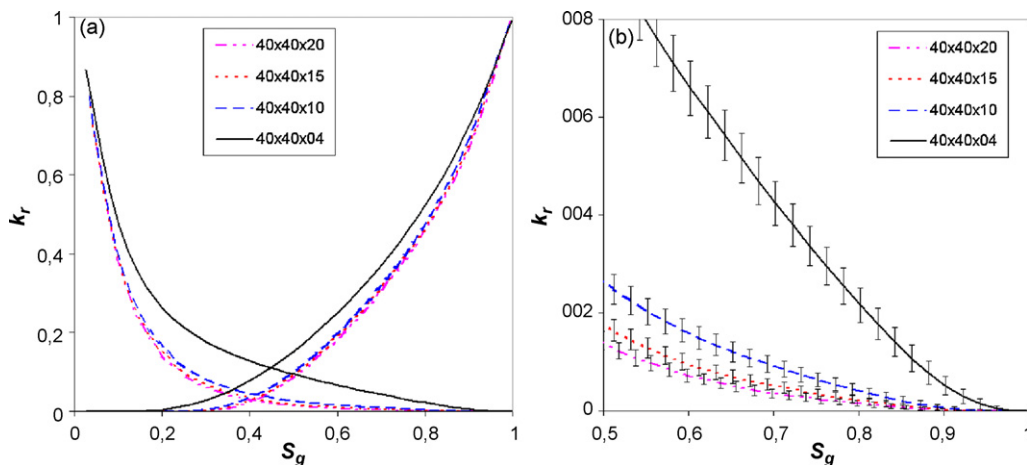

Fig. 6. (a) Influence of network thickness on relative permeability curves. (b) Detailed view for the high overall gas saturation, the error bars represent ± 1 standard deviation around the mean values over the number of realizations considered.
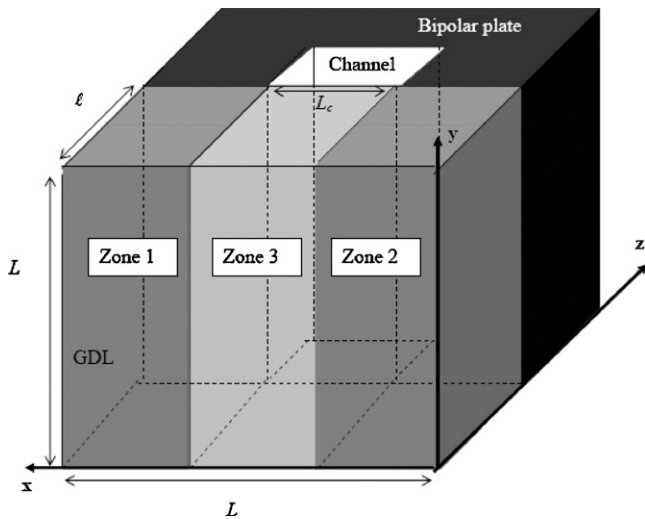
Fig. 7. Definition of various zones for the analysis of screen and differential compression effects. Zones 1 and 2 can be affected by mechanical compression whereas zone 3 is supposed to remain unperturbed.

less marked when the size varies from 10 to 15. Interestingly and contrary to the capillary pressure curve, the size effect is effective over most of the curve and not only in the vicinity of the high gas saturation. Again these results suggest that the relative permeabilities should be determined for the suitable size of thin system and that determination over systems larger than the one actually used in the application (here the fuel cell) is likely to introduce significant errors.

5. Impact of reduced exit area and compression effects

As sketched in Fig. 1, only a fraction Φ of the GDL unit cell exit surface, i.e. the surface of the GDL in contact with the bipolar plate, is actually in contact with the gas channel. Also, due to the bi-polar plate grooved structure, it is expected that the part of the GDL in contact with the channels is less mechanically compressed than the part in contact with the solid materials when the GDL is in place within the fuel cell. In continuation and complement to previous studies, e.g. [9,21,22] and references therein, the possible impact of these effects is explored in this section. Before presenting the results some definitions have to be given. Let L_c be the fraction of L corresponding to the channel (Fig. 1). The GDL unit cell exit surface open fraction is then given by $\Phi = L_c/L$. As

sketched in Fig. 7, three zones are distinguished in the GDL unit cell. Zones 1 and 2 are in contact with the bi-polar plate solid materials whereas zone 3 is located right underneath the channel. To simulate the effect of differential compression, the method is as follows. Starting from a given realization of the GDL unit cell, it is assumed that the compression only affects zones 1 and 2. In these zones, it is assumed that the main effect of compression (at least as regards the impact of compression on the liquid invasion) is to reduce the size d of a throat or a pore according to the simple rule: $d_{comp} = \alpha d$ where α is the compression coefficient with $0 < \alpha \leq 1$. Hence $\alpha = 1$ corresponds to the case without differential compression. All the results presented in this section are obtained for $N = 10$.

5.1. Overall saturation at breakthrough and saturation profiles

Fig. 8a shows the evolution of the average overall saturation in the unit cell as well as the overall saturation in the three zones as a function of Φ at breakthrough for $\alpha = 1$ (no differential compression). As expected $\langle S \rangle_{BT}$ increases with the fraction of the exit surface in contact with the solid materials. The saturation tends to be slightly higher in the zones located underneath the solid materials (zones 1 and 2). The effect of differential compression is depicted in Fig. 8b for $\Phi = 0.5$. We recall that the invading fluid invades preferentially the interfacial bonds of largest size (i.e. of smallest capillary pressure threshold) in the invasion percolation regime. As a result, the compressed zones are not visited at all with a sufficient compression. This suggests that the differential compression can be beneficial: liquid water would be transported in zone 3 (the less compressed zone) whereas the most compressed zones (zones 1 and 2) would contain no or significantly less water and therefore would offer zones where the gas transport is easier.

Fig. 9 shows how the saturation profile (along the thickness) is affected by the reduced exit area and the differential compression effect. These profiles are obtained by computing the saturation over successive slices of network for many realizations (the error bars in Fig. 9 correspond to ±1 standard deviation around the mean values). The profiles in Fig. 9 have the concave shape typical of IP profiles at breakthrough, e.g. [9] and references therein.

The effect of differential compression shown in Figs. 8b and 9b is fully consistent with what is expected if one considers, as here, that the net result of differential compression is purely geometrical and leads to more narrow throats and pores in the compressed zones. The situation may be actually subtler if one considers that the in-plane compression is different from the through plane com-
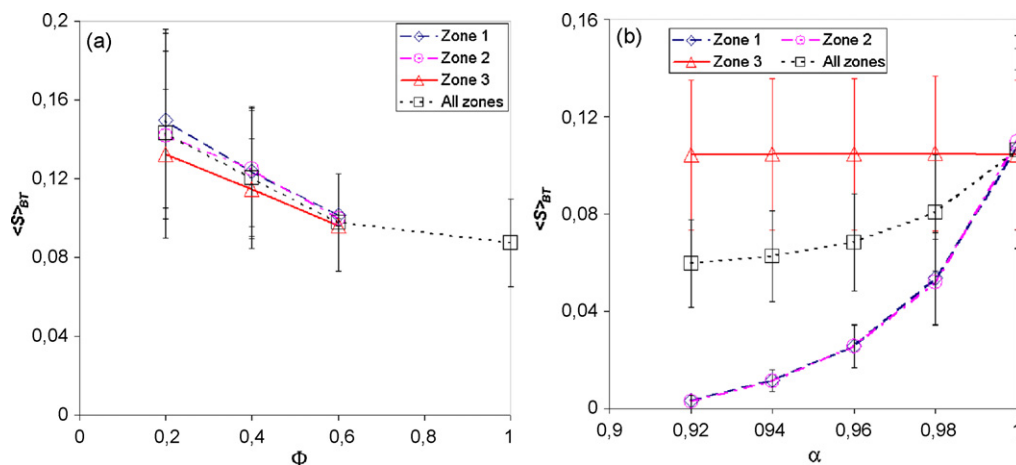

Fig. 8. (a) Evolution of overall saturation at breakthrouh in the different zones as a function of free outlet surface fraction (without differential compression, i.e. $\alpha = 1$), (b) evolution of overall saturation at breakthrouh as a function of differential compression factor α (for a free outlet surface fraction $\Phi = 0.5$).
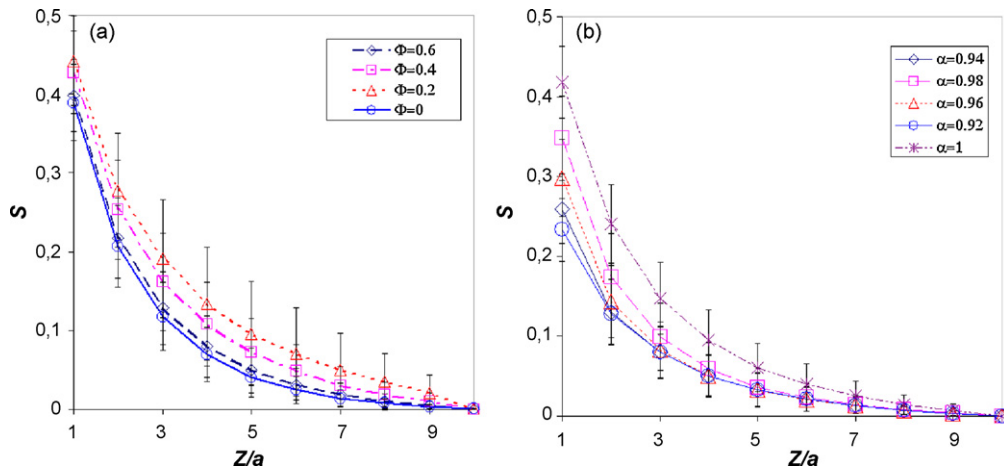
Fig. 9. Evolution of saturation profile at breakthrough (a) Effect of free outlet surface fraction ($\alpha = 1$). (b) Effect of differential compression ($\Phi = 0.5$).

pression and also if compression effects induced modification of local wettability conditions as suggested in [23].

5.2. Capillary pressure

The effect of differential compression on the apparent capillary pressure is shown in Fig. 10. As can be seen from Fig. 10, the capillary pressure curve is not affected for the high gas saturation. The capillary pressure increases with the compression in the range of intermediate saturations. This is obviously consistent with the fact that the sizes of throats located in the compressed zones are assumed to become narrower with the compression. Changing the outlet open surface fraction Φ in the absence of compression has no significant effect on $P_c(S)$ if one assumes, as we do in this paper, that trapping phenomena can be neglected.

5.3. Permeability and relative permeabilities

Fig. 11 shows the impact of reduced exit area and compression effect on apparent permeability. Contrary to the intrinsic permeability of the porous medium, which is supposed to be a local property of the porous microstructure, the apparent permeability characterizes the global permeability of the system formed by the GDL unit cell in the presence of the bipolar plate and associated effects of compression and reduced exit area. The apparent permeability can therefore be defined as

$$K_a = \frac{\mu Q}{(P_{en} - P_{ex})} \frac{\ell}{L^2} \tag{7}$$

where Q is the flow rate, P_{en} the pressure at the entrance of the system and P_{ex} the average pressure at the exit, i.e. in the channel at $z = \ell$.

As discussed in [23], the apparent permeability decreases when the exit area is reduced owing to the deformation of streamlines within the porous domain. This is exemplified in Fig. 11a for the particular system considered here. As depicted in Fig. 11b, the effect of differential compression on apparent permeability is not important over the range of compression factor investigated.

As shown in Fig. 12, the situation is quite different as regards the apparent relative permeabilities (defined as $k_{ra} = (\mu Q/K_a(P_{en} - P_{ex}))(\ell/L^2)$, where μ, Q and P are the dynamic viscosity, flow rate and pressure in the considered fluid), i.e. the main factor affecting the apparent relative permeabilities is the compression. This was expected since we know from Section 5.1 that the differential compression has a very significant effect on the liquid water distribution during the invasion with preferential invasion of the zone located under the channel for a sufficient compression.

6. Injection from an isolated source

For all the two-phase flow simulations presented so far, we have assumed that liquid water was present over the entire unit cell entrance surface and also supposed implicitly that the liquid pressure was uniform over this surface. As discussed in Section 3, this case can be representative of ex-situ experimental tests aiming at characterizing the GDL properties. However, the boundary condition for a GDL in a fuel cell could be different since water has to travel through the active layer and the MPL, if any, before reaching the GDL. Assume for example the presence of a MPL. The MPL pores are much smaller than GDL ones. Assume for simplicity that the water transfer within the MPL can also be described by IP (we recall that the MPL is hydrophobic which is consistent with the IP regime). Then water should break at the MPL/GDL interface through one pore of the MPL. According to this extreme case, this would imply that water enters the GDL unit cell through only one pore of the GDL entrance surface. It is likely that water enters in fact through several isolated pores since water is produced from many independent sources ($\approx$the platinum grains) in the active layers, but the details are still an open question. For the moment, we simply wish to explore the impact of a single injection source.
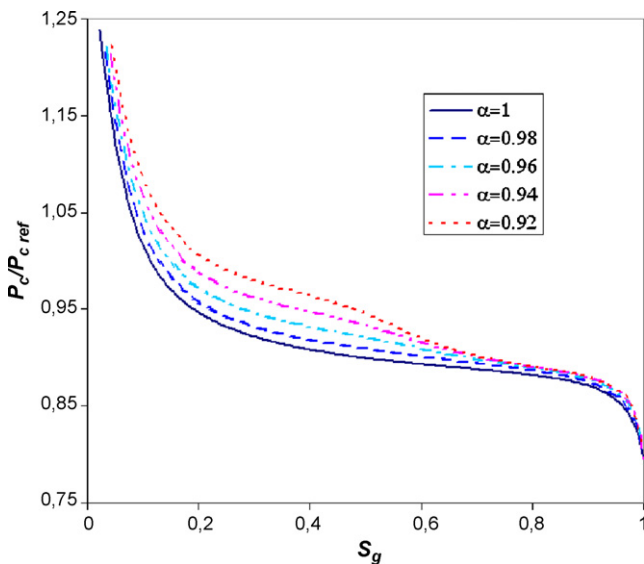

Fig. 10. Evolution of capillary pressure curve with compression factor α ($\Phi = 0.5$).
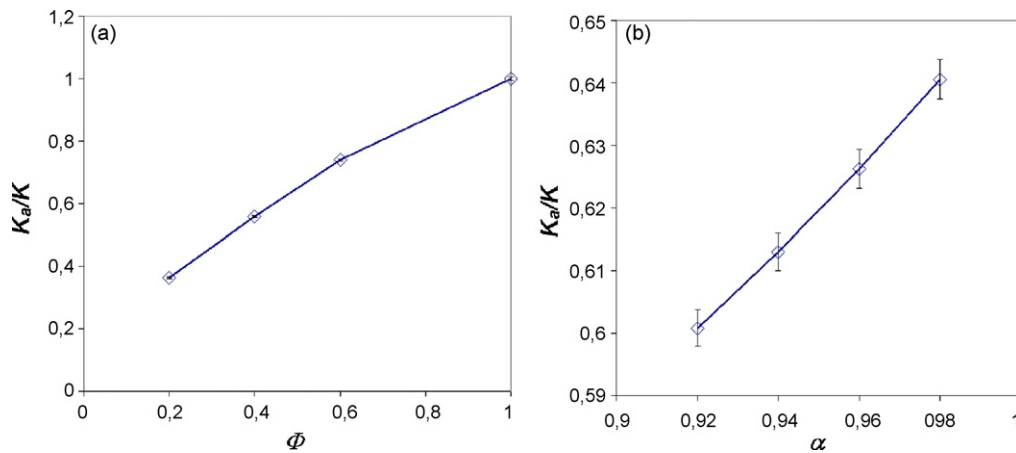
Fig. 11. (a) Evolution of apparent permeability as a function of free outlet surface fraction ($\alpha = 1$). (b) Evolution of apparent permeability as a function of differential compression ($\Phi = 0.5$).

Hence we assume that water invades the GDL from a single throat arbitrarily chosen as the throat located in the middle of the unit cell entrance surface. The water invasion simulations are still based on the IP algorithm and have been performed for $\Phi = 1$ and $\alpha = 1$, i.e. no restricted exit area, no compression. As shown in Fig. 4, the injection boundary condition has a significant impact on the overall saturation at breakthrough. As expected a smaller fraction of the pore space is invaded when water enters from an isolated local source. As can be seen from Fig. 4, $\langle S \rangle_{BT}$ increases quasi-linearly with the unit cell thickness N for the one point injection mode.

The saturation profiles at breakthrough for the two injection modes are compared in Fig. 13. Contrary to surface injection, the one-point injection leads to non-concave, non-monotonic profiles except for the thinnest systems considered for which the profile is almost flat. Hence the concave shape observed in the traditional IP simulations is strongly dependent on the boundary condition and this can contribute to explain why profiles deduced from in situ experiments, e.g. [24,25] are not concave. Also, it is clear from Fig. 13 that the one-point injection mode is significantly more favourable to gas transport since the gas saturation is higher everywhere along the profile.

7. Continuum model vs pore network model steady state saturation profiles

In this section we consider again the basic situation ($\Phi = 1$ and $\alpha = 1$) and compare the steady state saturation profile at break-through predicted on the one hand thanks to the IP algorithm on the pore network and on the other hand with the traditional continuum model. Following an approach similar to the one presented in [2], the continuum model leads to

$$\frac{IM}{2F} = \frac{Kk_{r\ell}}{\nu} \frac{\partial P_c}{\partial S} \frac{\partial S}{\partial z} \tag{8}$$

where $k_{r\ell}$ is the water relative permeability. Using ℓ as reference length, Eq. (8) is expressed in dimensionless form as

$$\frac{\partial S}{\partial Z} = -\frac{\ell}{\sqrt{K}} \frac{Ca}{\sqrt{\varepsilon}} \frac{1}{k_{r\ell}(\partial J/\partial S)} \tag{9}$$

where J is the Leverett function ($P_c = P_{water} - P_{gas} = (\gamma \cos \theta / \sqrt{K/\varepsilon}) J(S)$). Eq. (9) is solved using a classical fourth order Runge-Kutta method in conjunction with the boundary condition $S = S^*$ in $z = \ell$ ($Z = 1$). As an example, we consider the case of the $40 \times 40 \times 10$ system. Numerical fits of $J(S)$ and $k_{r\ell}(S)$ are deduced from the data reported in Figs. 5 and 6 for this system. One problem is to specify S^*, i.e. the boundary condition at $Z = 1$. An obvious option is to take $S^* = \langle S \rangle_{BT}$ since $k_{r\ell}(S) > 0$ only for $S \geq \langle S \rangle_{BT}$. Numerical tests show, however, that the saturation profile that is determined from Eq. (9) is not sensitive to the exact value chosen for S^* provided that the stepsize is sufficiently small and S^* is close to $\langle S \rangle_{BT}$.

The comparison between the saturation profiles determined using the IP algorithm and the one deduced from Eq. (9) (for two values of capillary number) is depicted in Fig. 14. As can be seen
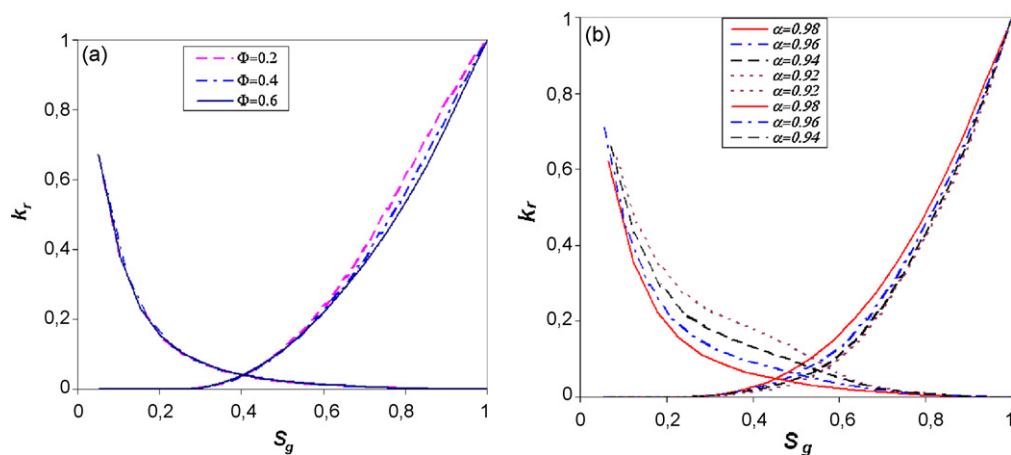

Fig. 12. Evolution of apparent relative permeabilities as a function of gas overall saturation (a) effect of free outlet surface fraction ($\alpha = 1$), (b) effect of differential compression ($\Phi = 0.5$).
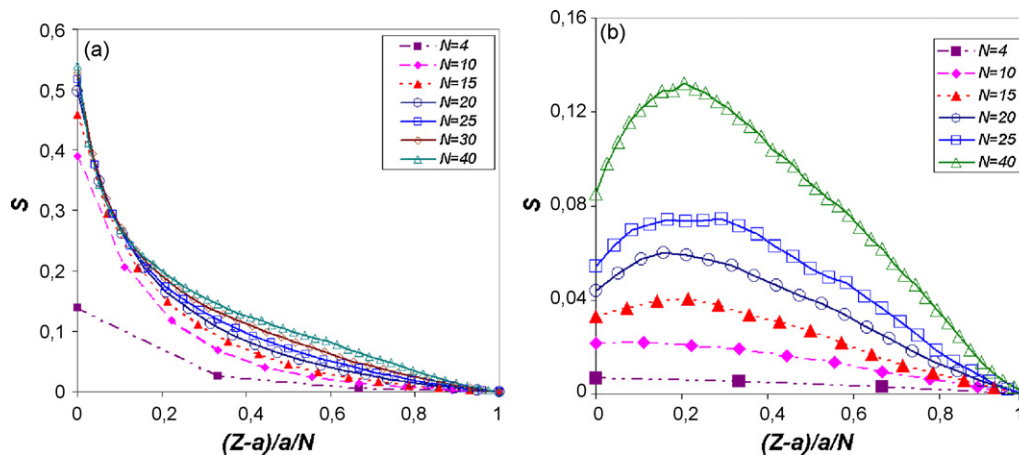
Fig. 13. Influence of injection boundary condition on the evolution of slice average liquid saturation along the network thickness. (a) Surface injection and (b) one point injection.

from Fig. 14, there are very significant differences between the IP profiles and the ones predicted with the continuum model. Note in particular the convex shape of profiles and above all the significantly higher saturations predicted in the second half of profiles with the continuum model. This was expected since it is widely admitted that the continuum model cannot describe the capillary fingering regime corresponding to IP. It is however interesting to see quantitatively in this example how wrong is the continuum model. This is discussed further in the next section.

8. Discussion

As illustrated in Fig. 14, predicting the GDL pore blockage by the water using the traditional continuum two-phase flow model is likely to lead to serious errors. One first problem is that the water invasion regime in a GDL is expected to correspond to the capillary fingering regime (see Section 2). This regime leads to fractal invasion patterns and cannot be described using the traditional continuum approach (the continuum approach to porous media is
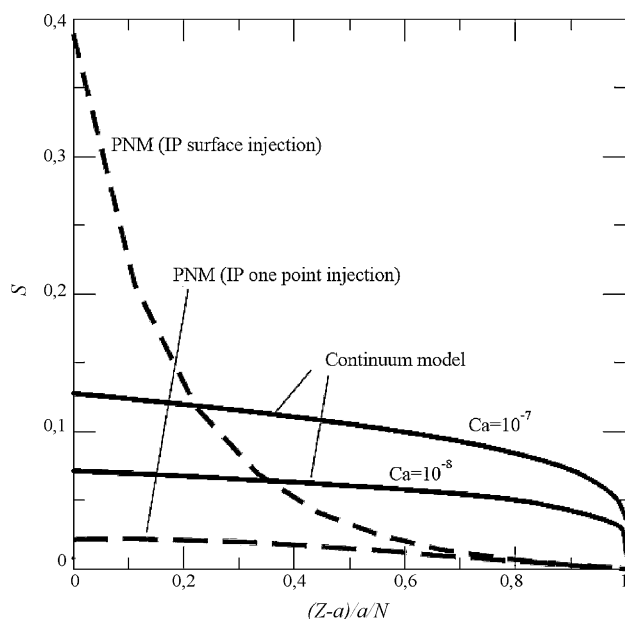

Fig. 14. Comparison of saturation profiles predicted using the pore network model (PNM) for the two boundary conditions sketched in Fig. 1 and the profile predicted with the continuum model.

conceptually based on the existence of Representative Elementary Volume, e.g. [26], and such a REV cannot be defined with a fractal distribution of the fluids).

A related problem is that a GDL is very thin (measured in pore size). As a result, it becomes questionable to use the traditional continuum model as a local model. For example the parameters ε, K, $k_{r\ell}$, $(\partial J/\partial S)$ in Eq. (8) are traditionally considered as local parameters, i.e. defined over a REV. In the case of the GDL unit cell considered in this paper, we face the odd situation in which the system size is on the order or even lower than the REV size. Under these circumstances, it becomes clearly doubtful to give its usual local meaning to the classical two-phase flow model. Hence, to obtain the profiles shown in Fig. 14, we have solved Eq. (8) as a local equation using parameters determined over the entire system, which is not at all in agreement with the traditional concept of length scale separation underlying the continuum model. The scale dependence of the parameters exemplified in Section 4 is another illustration of the lack of REV in the present context.

The fundamental differences between the continuum models and the IP approach can also be seen from the fact that the continuum model profiles are capillary number dependent whereas there are independent of viscous effects with the IP model (see Section 2). Also, as pointed out in [17], a boundary condition should be specified at the GDL/channel, i.e. the "local" saturation, with the continuum model whereas the IP model predicts this saturation, which therefore need not to be specified (this implies, however, that there is no limitation in the channel for evacuating the water reaching the channel from the GDL).

Owing to the lack of length scale separation, using the continuum model as a local model in 2D or 3D simulations so as to investigate for example the effect of the outlet restricted area at the GDL/channel interface is likely to lead to predictions still poorer than for the 1D case considered in Section 7.

Owing to the poor performances of continuum models, pore network models offer an attractive alternative. Yet there are several problems. As illustrated in Figs. 13 and 14, the IP-PNM prediction is quite sensitive to the injection boundary condition. Also, the conditions used in this paper lead to a single breakthrough point at the GDL/channel interface, which is not in agreement with the visualisation studies, e.g. [27], which rather indicate several breakthrough points, i.e. the formation of several droplets and not a single one over channel distances comparable to the GDL unit cell size considered in the present study. If viscous effects can be discarded as discussed in Section 2, this can be explained by either condensation effects within the GDL since the GDL is cooler than the active

layer or by the fact that liquid water enters the GDL through several independent injection points, [9,17].

Owing to the IP-PNM model sensitivity to the injection boundary condition (see Figs. 13 and 14), the question of the proper injection condition to be imposed at the GDL inlet surface appears as very important. As outlined in [17], it seems difficult to specify this condition without the full consideration of the water production and transfers in the GDL adjacent layers, i.e. the active layer and the MPL. Also, it is widely admitted that an increase in the current density should lead to an increase in the overall saturation of the GDL. Within the IP-PNM framework, this would mean an increase in the number of injection points.

Throughout this study we have assumed that the GDL was hydrophobic and that invasion could be simulated using the IP algorithm. As pointed out in [4], the IP algorithm is strictly valid only for sufficiently high contact angle (measured in the invading phase). For instance, the simulations shown in [4] for a 2D model system indicates that the invasion pattern is not strictly an IP one for contact angles representative of water on PTFE owing to changes in the liquid–gas interface local growth mechanisms, see [4] for more details. The range of contact angles for which the IP model becomes in serious error can be perfectly characterized for systems similar as the 2D ones considered in [4]. For a much more complex 3D microstructure like a GDL, this is an unexplored question.

Also, it seems to be more correct to consider a GDL as a system of mixed wettability rather than a purely hydrophobic system, e.g. [7,28,29]. Liquid invasion dominated by capillary effects in a system of mixed wettability cannot be described using the IP algorithm and more complex local invasion rules must be used, e.g. [4,7,29]. Hence, this aspect should be taken into account in the pore network simulations. However, it is, by no means, expected that the consideration of mixed wettability effects will change the conclusions of the present study regarding the poor predictions that can be expected from continuum models. The invasion process will be still dominated by capillary effects and the lack of length scale separation will be still present. We have also ignored the non-isotropic nature of the GDL microstructure. However, it is clear that almost all GDL types are highly anisotropic. Although this will not change the main results of the present study, the influence of GDL anisotropy on liquid invasion would deserve to be studied in some details in a future work.

9. Conclusion

As illustrated in this paper, the traditional continuum models widely used for describing two-phase flow in GDLs should be considered as leading to only poor approximations of water distribution in the GDL.

The main reasons of the continuum model poor performances are the lack of length scale separation (which, among other things, leads to scale dependent transport properties) and the fact that the invasion regime is dominated by capillary effects (this introduces a second lack of length scale separation owing to the phases fractal distribution corresponding to the capillary fingering regime). In other terms, the condition underlying the continuum approach to porous media, i.e. the existence of a representative elementary volume of size much smaller than the porous domain, is not met in a GDL.

Due to the limitations of continuum models, pore network models (PNMs) appear as a good trade-off between accuracy and computational effort.

However, several aspects related to the use of PNMs needs to be clarified. This notably includes the injection condition and a better assessment of wettability related effects (relevance of IP model for contact angles representative of water on PTFE, mixed wettability).

Also, since the invasion pattern is strongly dependent on the injection boundary condition, this study suggests that a proper analysis of water transport in a GDL cannot be performed without consideration of water generation and transport in the adjacent porous layers (active layer and MPL).

References

[1] J.H. Nam, M. Kaviany, Int. J. Heat Mass Transfer 46 (2003) 4595–4611.
[2] U. Pasaogullari, C.Y. Wang, J. Electrochim. Soc. 151 (2004) A399–A406.
[3] J. Hermann, C. Ziegler, J. Electrochim. Soc. 155 (10) (2008) B1066–B1076.
[4] O. Chapuis, M. Prat, M. Quintard, E. Chane-Kane, O. Guillot, N. Mayer, J. Power Sources 178 (2008) 258–268.
[5] X.D. Niu, T. Munekata, S.A. Hyodo, K. Suga, J. Power Sources 172 (2007) 542–552.
[6] J.T. Gostick, M.A. Ioannidis, M.W. Fowler, M.D. Pritzker, J. Power Sources 173 (2007) 277–290.
[7] P.K. Sinha, C.Y. Wang, Chem. Eng. Sci. 63 (2008) 1081–1091.
[8] A. Bazylak, V. Berejnov, B. Markicevic, D. Sinton, N. Djilali, Electrochim. Acta 53 (2008) 7630–7637.
[9] K.J. Lee, J.H. Nam, C.J. Kim, Electrochimica Acta 54 (2009) 1166.
[10] F. Barbir, PEM Fuel Cells: Theory and Practice, Elsevier Academic Press, 2005.
[11] G. Inoue, T. Yoshimoto, Y. Matsukuma, M. Minemoto, J. Power Sources 175 (2008) 145–158.
[12] F.A.L. Dullien, Porous Media. Fluid Transport and Pore Structure, Academic Press, 1991.
[13] R. Lenormand, E. Touboul, C. Zarcone, J. Fluid Mech. 189 (1988) 165–187.
[14] Y. Yortsos, B. Xu, D. Salin, Phys. Rev. Lett. 79 (23) (1997) 4581–4584.
[15] R. Lenormand, Proc. R. Soc. Lond. A 423 (1989) 159–168.
[16] D. Stauffer, A. Aharony, Introduction to Percolation Theory, Taylor & Francis, London, 1992.
[17] J.H. Nam, K.J. Lee, G.S. Hwang, C.J. Kim, M. Kaviany, Int. J. Heat Mass Transfer (2009), in press.
[18] S. Litster, D. Sinton, N. Djilali, J. Power Sources 154 (2006) 95–105.
[19] J. Hoshen, R. Kopelman, Phys. Rev. B 14 (8) (1976) 3438–3445.
[20] M.J. Blunt, M.D. Jackson, M. Piri, P.H. Valvatne, Adv. Water Resour. 25 (2002) 1069–1089.
[21] P.K. Sinha, C.Y. Wang, Electrochem. Acta 52 (2007) 7936–7945.
[22] A. Bazilak, D. Sinton, Z.S. Liu, N. Djilali, J. Power Sources 163 (2007) 784–792.
[23] J. Dufrêche, M. Prat, P. Schmitz, J.D. Sherwood, Chem. Eng. Sci. 57 (2002) 2933–2944.
[24] M.A. Hickner, N.P. Siegel, K.S. Chen, D.S. Hussey, D.L. Jacobson, M. Arif, J. Electrochem. Soc. 155 (2008) B427.
[25] C. Hartnig, I. Manke, R. Kuhn, N. Kardjilov, J. Banhart, W. Lehnert, Appl. Phys. Lett. 92 (2008) 134106.
[26] J. Bear, Y. Bachmat, Introduction to Modeling of Transport Phenomena in Porous Media, Kluwer Academic Publishers, 1990.
[27] T. Ous, C. Arcoumanis, J. Power Sources 173 (2007) 137–148.
[28] J.T. Gostick, M.W. Fowler, M.A. Ioannidis, M.D. Pritzker, Y.M. Volfkovich, A. Sakars, J. Power Sources 156 (2006) 375–387.
[29] H. Chraibi, L. Ceballos, M. Prat, M. Quintard, A. Vabre, Proceedings of Fundamentals & Developments of Fuel Cells (FDFC) 2008 Conference, Nancy, 10–12th, 2008.